

Article

Study on Water Inrush Characteristics of Hard Rock Tunnel Crossing Heterogeneous Faults

Guoxu Xin ¹, Bo Wang ^{1,2,3,4,*}, Haozhang Zheng ³, Linfeng Zeng ¹ and Xinxin Yang ⁵

¹ State Key Laboratory of Intelligent Construction and Healthy Operation and Maintenance of Deep Under-Ground Engineering, China University of Mining and Technology, Xuzhou 221116, China; guoxuxin2019@163.com (G.X.); ts21010007a31@cumt.edu.cn (L.Z.)

² School of Resources and Geosciences, China University of Mining and Technology, Xuzhou 221116, China

³ School of Mechanics and Civil Engineering, China University of Mining and Technology, Xuzhou 221116, China; haozhang.zheng@griffithuni.edu.au

⁴ YunLong Lake Laboratory of Deep Underground Science and Engineering, Xuzhou 221116, China

⁵ Beijing Urban Construction Design & Development Group Co., Limited, Beijing 100045, China; 13485347840@163.com

* Correspondence: wbsyes@126.com

Abstract: Fault water inflow is one of the most severe disasters that can occur during the construction of hard and brittle rock tunnels. These tunnels traverse brittle fault breccia zones comprising two key components: a damage zone dominated by low-strain fractures and an internally nested high-strain zone known as the fault core. Structural heterogeneity influences the mechanical and hydraulic properties within fault breccia zones, thereby affecting the evolving characteristics of water inflow in hard rock faulting. Based on the hydraulic characteristics within hard rock fault zones, this paper presents a generalized dual-porosity fluid-solid coupling water inflow model. The model is utilized to investigate the spatiotemporal evolution patterns of water pressure, inflow velocity, and water volume during tunneling through heterogeneous fault zones in hard rock. Research findings indicate that when tunnels pass through the damage zones, water inrush velocity is high, yet the water volume is low, and both decrease rapidly over time. Conversely, within the core regions of faults, water inflow velocity is low, yet the water volume is high, and both remain relatively stable over time. Simulation results closely align with the water inflow data from China's largest cross-section tunnel, the Tiantai Mountain Tunnel, thus validating the accuracy of the evolutionary model proposed in this paper. These findings offer a new perspective for devising effective prevention strategies for water inflow from heterogeneous faults.

Keywords: hard rock tunnel; water-rich fault; heterogeneous faults; generalized dual porosity model; stress-seepage coupling



Citation: Xin, G.; Wang, B.; Zheng, H.; Zeng, L.; Yang, X. Study on Water Inrush Characteristics of Hard Rock Tunnel Crossing Heterogeneous Faults. *Appl. Sci.* **2024**, *14*, 2536. <https://doi.org/10.3390/app14062536>

Academic Editor: Stefano Invernizzi

Received: 12 February 2024

Revised: 8 March 2024

Accepted: 9 March 2024

Published: 17 March 2024



Copyright: © 2024 by the authors. Licensee MDPI, Basel, Switzerland. This article is an open access article distributed under the terms and conditions of the Creative Commons Attribution (CC BY) license (<https://creativecommons.org/licenses/by/4.0/>).

1. Introduction

In recent years, driven by China's economic and technological development, the construction of tunnels has been shifting from shallow-buried soft rock tunnels to deeply-buried hard brittle rock tunnels [1,2]. Hard brittle rocks can provide high strength and overall stability for deep engineering projects [3]. However, under the influence of tectonic stress, they are also prone to generating numerous brittle fracture zones [4]. These geological formations serve as crucial pathways for fluid flow in the upper crust [5–7]. Once tunnel excavation exposes these formations, groundwater trapped within them flows into the tunnel, leading to severe water inflow disasters [8]. Statistics reveal that nearly all hard rock tunnels have been affected by fault water inflow, resulting in direct economic losses amounting to billions of yuan. Therefore, revealing the characteristics of water inflow caused by traversing water-rich fault zones in hard and brittle rock tunnels holds significant importance for the current stage of tunnel engineering development in China.

Researchers have conducted extensive research on the evolution mechanisms of water gushing and mud gushing during tunnel excavation in hard-brittle fault breccia belts. These efforts have yielded valuable insights. Masset O., et al. [9] conducted a comprehensive analysis of 23 cases of water surges in hard and brittle rock tunnel faults in the Alps, revealing a correlation between the rate of water surges and rock properties. KC D., et al. [10] reviewed three significant tunnel projects in the Himalayan region, analyzing the adverse effects of continuous surface water supply and tectonics on construction. Nielsen summarized the construction experience of nearly 50 typical hard rock subsea tunnels in Norway, and found the main characteristics of fault water gushing and significant deformation of hard rock tunnels [11–13]. At the laboratory scale, similar physical simulation experiments can more intuitively observe the disaster process and evolution mode of fault water inflow in deep tunnel scenarios [14,15]. Huang Z., et al. [16] developed a model experimental system to simulate tunnel excavation and water injection for inrush, utilizing Acoustic Emission (AE) for positioning and monitoring the evolution of inrush channels in the surrounding rock during the water supply process. In recent years, with the advancement of computer technology, more and more researchers use numerical simulation methods to study the phenomenon of fault water gushing. Using FEM to discretize faults is the most common method for studying water inrush disasters [17–20]. Yang W.M., et al. [21] elucidated the process of water inrush in deep tunnels by establishing a finite element model. Zhang J., et al. [22] conducted a study on the fluid-structure interaction effect of water inrush from water-rich faults using COMSOL Multiphysics software. In recent years, with the advancement of numerical calculation methods, the Discrete Element Method (DEM) and Smoothed Particle Hydrodynamics (SPH) have been applied to tackle water inrush issues in fractured rock tunnels [23,24]. Fan. H.Y., et al. [25] coupled SPH with the Discontinuous Deformation Analysis (DDA) method to simulate the fluid motion state in fault water inrush disasters.

The above research is of great significance for advancing the research on the mechanism of cement gushing flow in tunnels. In these studies, fault zones are generally assumed to be homogeneous and isotropic. However, fault breccia zones in hard-brittle rock formations exhibit a heterogeneous structure [26–28]. Extensive field observations have shown that the brittle fracture zone consists of a high-strain core region and an outer low-strain fracture network region, called the damage zone (Figure 1) [29,30]. This structural change results in complex hydraulic behavior within the fault zone [31,32]. Studies of the Eika-Müllers Tunnel have shown that the heterogeneity of the fault zone within the granite leads to highly inhomogeneous permeability distributions and affects water inflow within the tunnel [33]. However, changes in the evolution pattern of water ingress characteristics caused by heterogeneity are still unclear.

Qinling Tiantai Mountain Tunnel is the largest hard rock tunnel in China in terms of sections. A number of serious fault water inrush disasters occurred during the tunnel's construction. First, by analyzing the differences in mechanical and flow characteristics within faults due to heterogeneity, a generalized dual-porosity fluid-structure interaction model was established. Second, based on the hydrogeological conditions of the Tiantai Mountain Tunnel, a numerical calculation model was developed. Finally, by integrating numerical simulations with field measurement results, the study examined the dynamic evolution of water inflow rate and volume when the tunnel crosses heterogeneous faults.

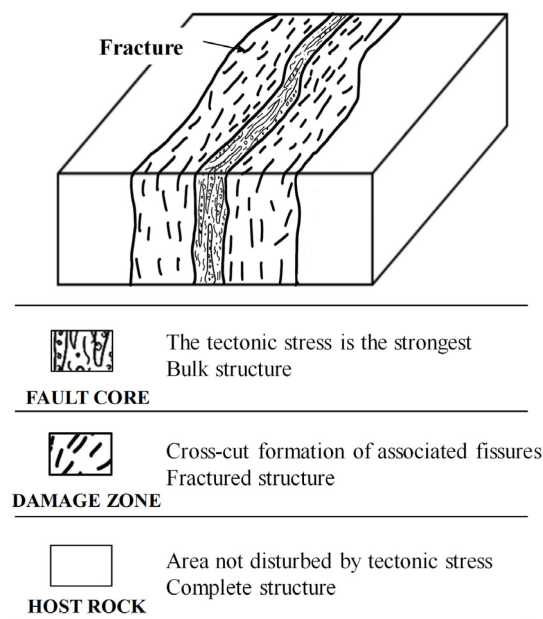


Figure 1. Internal structure of heterogeneous faults.

2. Geological Setting of Tiantai Mountain Tunnel

A strategically significant position within China's G85 highway is occupied by the Tiantai Mountain Tunnel, encompassing a total length of 15.56 km. Presently, it ranks among the largest cross-sectional tunnels in Asia, characterized by a two-way configuration housing six lanes. With a maximum cross-sectional area of 156 m² and an average depth of 1117 m, this tunnel serves as an exemplar of the typical characteristics exhibited by deeply buried long-section mountain tunnels. In this paper, the chainage interval from K159 + 285 to K164 + 350 has been chosen for study.

Due to its significant depth, the tunnel traverses through unweathered granite formations, which have an average thickness of up to 810 m. In areas unaffected by faults, unweathered granite has excellent self-stabilizing capabilities and very low permeability. Above the unweathered formations lies moderately weathered granite with an average thickness of 300 m. According to on-site drilling data, the moderately weathered formation has a Rock Quality Designation (RQD) value of 30, with well-developed joint fractures that provide conditions for groundwater recharge [34].

2.1. Geological Structure

Under the influence of structural stress and compressive strain, large, medium, small, and micro faults develop obviously in the tunnel area, as shown in Figure 2. This study focuses on investigating the occurrence of water inrush in igneous rock tunnels intersected by the F6 fault. The F6 fault intersects the centerline of the tunnel at K160 + 880, with an azimuth of 75°. The F6 fault is exposed at the surface and penetrates through moderately weathered and unweathered strata. Through drilling and geophysical exploration, it has been found that within this fault segment there is a damage zone of about 60 m, along with a 2 m wide fault core area. Within the damage zone, a network of mesoscale fractures has developed, significantly deteriorating the mechanical properties of the granite and enhancing the water storage capacity of the area. There are no signs of mylonitization or shale formation within the fault core, which exhibits good hydraulic conductivity. Moreover, as the fault penetrates the entire moderately weathered stratum, it enhances the fault's capacity to receive surface recharge water from the moderately weathered layer, increasing the risk of water inrush in the tunnel.

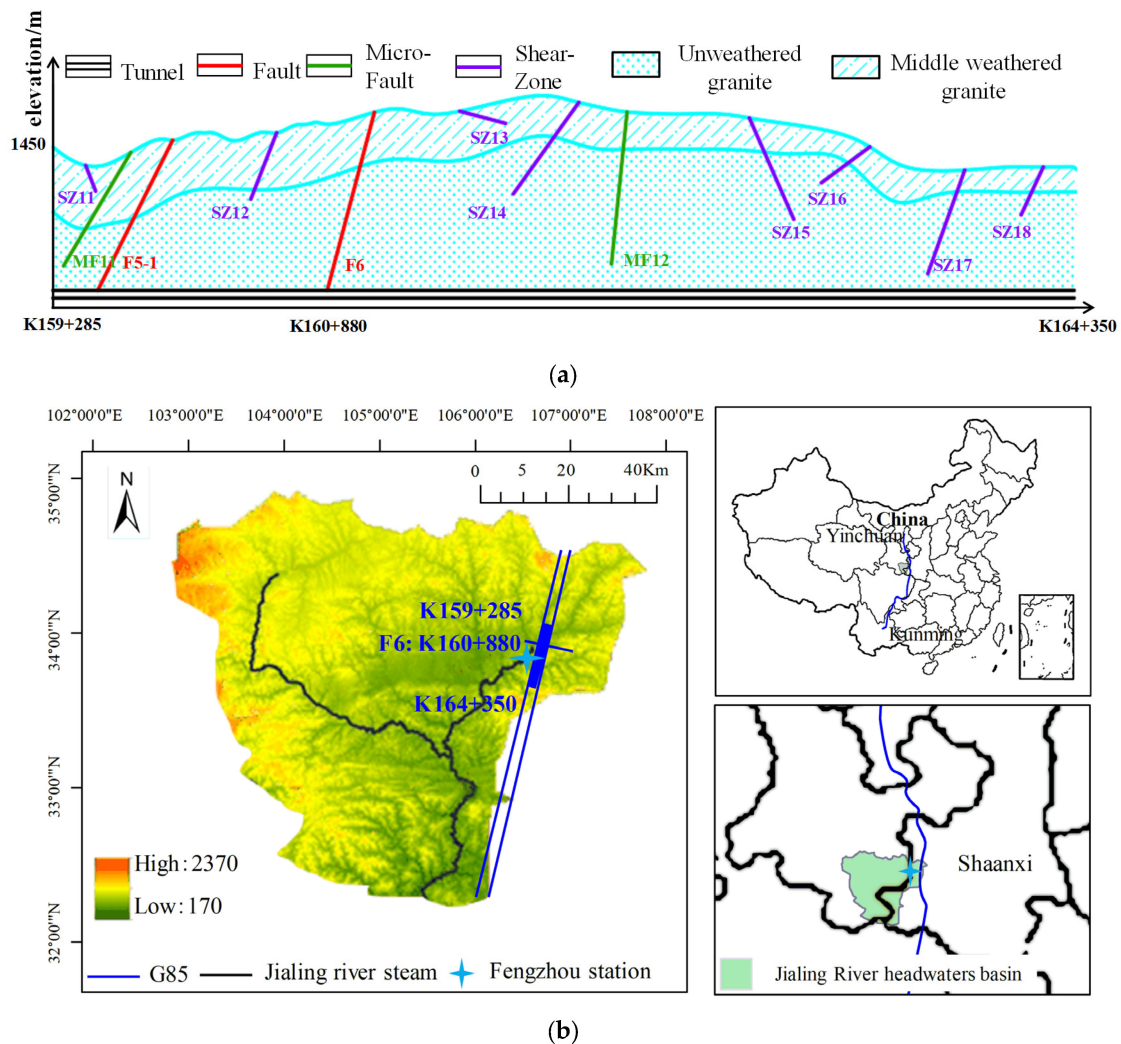


Figure 2. Hydrogeological conditions of the Tiantai Mountain Tunnel, the largest cross-section tunnel in China: (a) geological profile of the study section; (b) correlation between the tunnel area and the Jialing River headwaters basin.

2.2. Hydrologic Conditions

The tunnel site is in close proximity to the source of the Jialing River in China. The Jialing River is the largest river basin among the tributaries of the Yangtze River, the world's largest river in terms of hydroelectric energy (Figure 2). Hence, the surface water system in this area is relatively complex. Specifically, at K161 + 020, near the surface exposure of the F6 fault, there is a gully adjacent to a small tributary of the Jialing River. This tributary receives a continuous supply of surface water throughout the year. According to hydrological data observed at the Fengzhou station, located at the source of the Jialing River, the annual average underground runoff in this region is $0.005 \text{ m}^3/\text{s}$.

3. Fault Water Inrush Model of Igneous Rock

A generalized dual-porosity fluid-solid coupling model is established for the fault zone in this section. In this model, the damage zone is represented as a continuum with low conductivity and high storability, while the fault core is represented as a continuum with high conductivity and high storability. Both models employ Darcy's law for flow and transport, utilizing the advection-diffusion equation.

3.1. Control Equations for Fault Core

Intensified stress concentration in the fault core area results in the absorption of a significant amount of energy and deformation, leading to the scattered distribution of rock mass within the fault core, as shown in Figure 3a [35]. According to the correlation between representative volume element (REV) and engineering scale, the continuum model (CM) is used to study the solid deformation and fluid seepage patterns in the fault core.

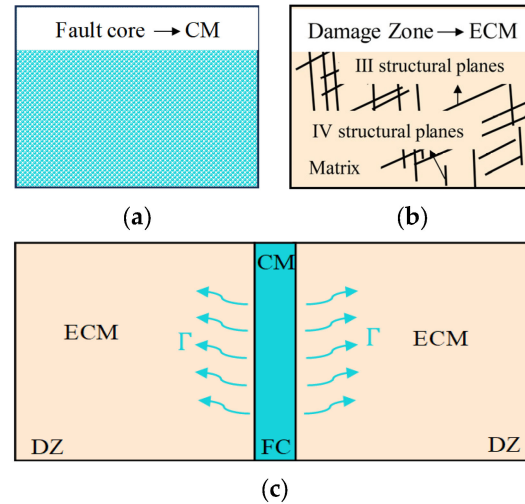


Figure 3. Generalized dual porosity coupling model: (a) continuum model (CM) at fault core (FC); (b) equivalent continuum model (ECM) at damage zone (DZ); (c) generalized dual continuum model in heterogeneous water-rich fault zones.

The equation for stress equilibrium in saturated fluid is as follows:

$$\nabla \cdot (\sigma_{fc} - \alpha_{fc} p \mathbf{I}) + \mathbf{f} = \mathbf{0} \quad (1)$$

where σ_{fc} is the stress, α_{fc} is the Biot's coefficient, p is the pore pressure, \mathbf{I} is the second-order unit tensor, and \mathbf{f} is the body force vector. The constitutive law of the fault core is:

$$\sigma_{fc} = \mathbf{C} : \boldsymbol{\varepsilon} \quad (2)$$

where \mathbf{C} is the solid skeleton stiffness tensor, $\boldsymbol{\varepsilon} = \nabla^s \cdot \mathbf{u}$ is the linearized strain tensor, and \mathbf{u} is the displacement for the solid matrix.

In this section, the Darcy model is employed to simulate the overall seepage field within the fault fracture zone. The Darcy model is chosen due to its ability to balance accuracy and computational efficiency, making it more suitable for engineering-scale seepage simulation research when compared to the Navier–Stokes flow model [23].

The continuity equation for single-phase fluid flow in continuous media is given by [36]:

$$\nabla \cdot - \frac{k_{fc}}{\mu_w} (\nabla p - \rho_w g) + \left(\frac{\alpha_{fc} - \varphi_{fc}}{K_{fc}} + \frac{\varphi_{fc}}{K_w} \right) \frac{\partial p}{\partial t} + \alpha_{fc} \frac{\partial \varepsilon_v}{\partial t} = W \quad (3)$$

where, k_{fc} is the permeability of the fault core; μ_w is the fluid viscosity, ρ_w is the fluid density, $\frac{\alpha_{fc} - \varphi_{fc}}{K_{fc}}$ is the compression term of rock skeleton; $\frac{\varphi_{fc}}{K_w}$ is the compression term of fluid; K_{fc} , K_w is the bulk modulus of the fault core and fluid respectively; φ is the porosity; $\alpha_{fc} \frac{\partial \varepsilon_v}{\partial t}$ is the volumetric strain term; and W is the source term.

Under the assumption of incompressible fluid, the equation of motion is given by Darcy's law as:

$$\mathbf{v} = -\frac{k_{fc}}{\mu_w} \nabla p \quad (4)$$

Based on the results of Louis's experiment, cross coupling term between the above two equations is as follows [37]:

$$k_{fc} = k_{fc0} e^{\lambda(\sigma_{fc} - \alpha_{fc} p)} \quad (5)$$

where k_{fc0} is the initial permeability of the fault core and λ is the influence coefficient.

3.2. Control Equations for the Damage Zone

The fault failure zone serves as a transition zone that connects the fault core with the surrounding rock. It is typically formed by the intersection of III and IV structural planes, spanning a range of 10–100 m, and represents a common type of fractured medium [38–40] (Figure 3b). The Equivalent Continuum Method (ECM) is a widely used theoretical approach to studying the hydraulic properties of fractured rock masses. Within ECM, the matrix, fractures, and pores are treated as a unified continuum. ECM offers several advantages, including simplified data requirements and low computational costs.

An equivalent set of fluid-solid coupling equations for damage zone is given by:

$$\nabla \cdot (\sigma_{dz} - \alpha_{dz}^{equ} p \mathbf{I}) + \mathbf{f} = \mathbf{0}, \sigma_{dz} = \mathbf{C}_{dz}^{equ} : \varepsilon \quad (6)$$

$$\nabla - \frac{k_{dz}^{equ}}{\mu_w} (\nabla p - \rho_w \mathbf{g}) + \left(\frac{\alpha_{dz}^{equ} - \phi_{dz}^{equ}}{K_{dz}^{equ}} + \frac{\phi_{dz}^{equ}}{K_w} \right) \frac{\partial p}{\partial t} + \alpha_{dz}^{equ} \frac{\partial \varepsilon_v}{\partial t} = \Gamma \quad (7)$$

$$\mathbf{v}_{dz} = -\frac{k_{dz}^{equ}}{\mu_w} \nabla p_{dz} \quad (8)$$

$$k_{dz}^{equ} = k_{dz0}^{equ} e^{\lambda(\sigma_{dz} - \alpha_{dz}^{equ} p)} \quad (9)$$

where the subscript dz means the homogenized fault damage zone, the superscript equ means the equivalent parameters, and Γ is the flow into the damage zone. The calculation of equivalent parameters \mathbf{C}_{dz}^{equ} , α_{dz}^{equ} , K_{dz}^{equ} , and k_{dz}^{equ} can be found in the reference [41].

3.3. Governing Equation for Global Seepage

The dual-porosity model is based on the concept that a fractured porous medium consists of two distinct regions with contrasting characteristics [42]. One region contributes significantly to permeability but has limited capacity, while the other region has low permeability but determines the overall capacity. In the case of the igneous rock fault fracture zone, the fault core acts as a pathway for groundwater flow, enhancing the permeability and conductivity of the fault. However, it has a narrow width and limited water storage capacity. On the other hand, the medium-scale fracture network within the damage zone has lower permeability but facilitates local water storage and communication [43,44]. Hence, the hydrological conditions within the fault meet the criteria for the generalized dual-porosity model, as shown in Figure 3c. By employing the concept of extended dual-porosity media, the governing equations for global seepage within the fault can be derived.

A separate Darcy's equation for each medium can be written as:

$$\mathbf{q}_{fc} = -\mathbf{k}_{fc} \frac{\partial p_{fc}}{\partial \mathbf{x}_j}; \mathbf{q}_{dz} = -\mathbf{k}_{dz}^{equ} \frac{\partial p_{dz}}{\partial \mathbf{x}_j} \quad (10)$$

where q_{fc} and q_{dz} are the fluid flow in the fault core and damage zone, respectively. The fluid mass balance, accounting for the fluid flow in the fault core (fc) and the damage zone (dz) as well as the interporosity fluid transfer, can be expressed separately as:

$$\frac{\partial \zeta_{fc}}{\partial t} + v^I \frac{\partial q_{fc}}{\partial x} = \Gamma \quad (11)$$

$$\frac{\partial \zeta_{dz}}{\partial t} + v^{dz} \frac{\partial q_{dz}}{\partial x} = -\Gamma \quad (12)$$

where $\Gamma = \Lambda(p_{fc} - p_{dz})$ represents the interporosity fluid flux transfer, Λ is a characteristics of fractured formation such as matrix's permeability, fractures' geometry, distribution, and size. ζ represents the fluid mass in the pore space, and $\zeta = \left(\frac{\Delta m_f}{\rho_{f,0}}\right) = -\alpha_{ij}\epsilon_{ij} + \frac{p}{M}$, M is the Biot's modulus.

4. Model Setup

The one-way section of the tunnel has a diameter of 12 m. Based on previous studies on boundary effects, the distance between the boundary of the affected area and the center of the tunnel section is three times the section diameter [22]. Assuming symmetry of the longitudinal section of the tunnel, only half of the numerical model needs to be built, with dimensions of 180 m × 80 m × 50 m. The F6 fault has a dip angle of approximately 75°, with a fault damage zone width of around 60 m and a fault core width of 2 m. In the model, all elements are divided into hexahedral solid elements with 8 nodes each, resulting in a total of 12,883,900 elements.

The Tiantai Mountain Tunnel has an average burial depth of 1000 m. Ground stress measurements indicate that the values of σ_x , σ_y , and σ_z are 15 MPa, 20 MPa, and 18 MPa, respectively. Taking into account the overall control effect of the fault core on the fluid domain within the fault zone [45], the boundary for the origin term is defined at the fault core. Based on the annual average underground runoff measured at the Fengzhou station, the source term is set at 0.005 m³/s. This study disregards the influence of the tunnel lining and solely focuses on the evolution of fault water inrush characteristics. After excavation, the cave wall and the tunnel face were provided with a permeable boundary. The numerical model is shown in Figure 4.

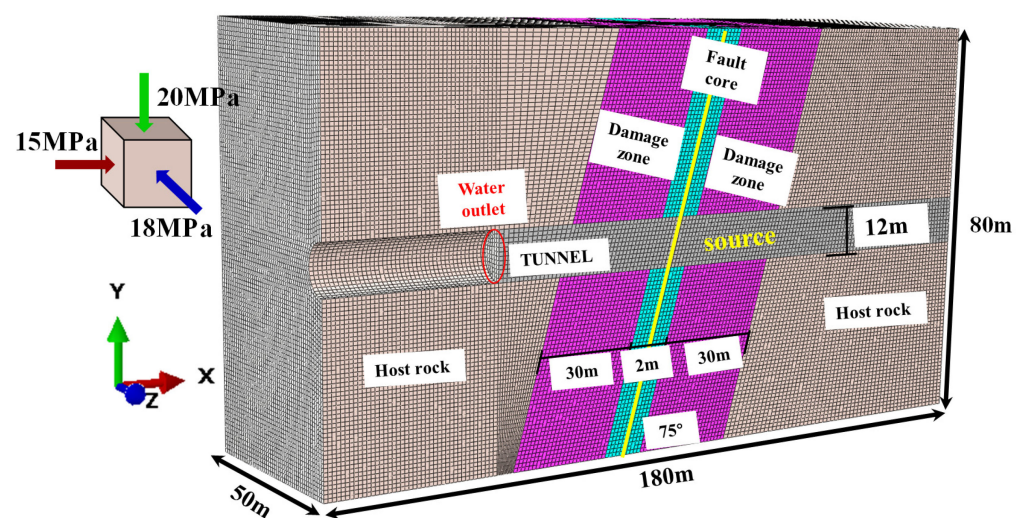


Figure 4. ABAQUS Numerical Model.

Field sampling results indicate that the uniaxial compressive strength (UCS) of intact granite is $\sigma_c = 158.35$ MPa, while the tensile strength of intact granite is $\sigma_t = 37.80$ MPa. Determining the overall mechanical properties of the rock mass within the damage zone

remains a challenging task in rock mechanics [46], due to the rocks at the fault core being too fragmented to measure their uniaxial compressive strength directly. For consistency, Hoek's Geological Strength Index (GSI) system was used to provide indirect estimates of rock mechanical properties in the damage zone and fault core. According to the GSI diagram, the GSI for the damage zone is 75, while the GSI for the fault core is 45. By referring to the relevant reference [46], the mechanical parameters can be calculated. Permeability coefficients have been selected based on references [47]. Table 1 provides a summary of the parameters required for the calculations.

Table 1. Calculation parameter table.

Zone	Material Properties	Value	Units
Fault core	The bulk modulus of elasticity K_{fc}	60,000	Mpa
	Initial permeability k_{fc0}	1.0×10^{-5}	m^2
	Porosity φ_{fc}	0.5	1
	Biot's coefficient α_{fc}	0.75	1
Damage zone	The equivalent bulk modulus of elasticity K_{dz}^{equ}	2000	Mpa
	Equivalent initial permeability k_{dz}^{equ}	2.48×10^{-8}	m^2
	Equivalent porosity φ_{dz}^{equ}	1.0×10^{-4}	1

5. Results

In this section, the generalized dual-porosity hydraulic inrush model is employed to investigate osmotic pressure, water inrush velocity, and water inrush volume of the tunnel face during the process of crossing the fault. The non-linear finite element software ABAQUS 2021 is utilized for the analysis. The obtained data are then compared with field-measured data for validation and verification purposes.

5.1. Evolution Law of Pressure

Figure 5 illustrates the evolution of the osmotic pressure field during the tunnel traversal. As depicted in Figure 5a, the pore pressure within water-rich faults decreases radially from the fault core towards the damage zone. With an external source term of $0.005 \text{ m}^3/\text{s}$, the maximum pore pressure reaches 10.5 MPa. When the tunnel face enters the fault zone, the flow boundary conditions are altered, leading to the formation of a "bullet-shaped" pressure drop zone around the tunnel, as observed in Figure 5b.

In ABAQUS, direct output of the fluid pressure gradient ∇p for each fluid cell is not available. Therefore, to calculate the pressure gradient vector ∇p at a specific fluid point (x_0, y_0, z_0) defined by the osmotic pressure function $p(x, y, z)$, the following expression can be used:

$$\nabla p = \left[p'_x(x_0, y_0, z_0), p'_y(x_0, y_0, z_0), p'_z(x_0, y_0, z_0) \right]^T \quad (13)$$

When $z = 0$, the pressure gradient ∇p simplifies to: $\nabla p = \left[p'_x(x_0, y_0), p'_y(x_0, y_0), 1 \right]^T$.

Using $(x, y) = (60, 5)$ as the origin of the coordinate system, a temporary Cartesian coordinate system $x'o'y'$ is established around the tunnel. Within this coordinate system, two osmotic pressure contours, namely L_i^{DZ} and L_i^{FC} , are extracted from the $x = 70 \text{ m}$ damage zone and the $x = 90 \text{ m}$ fault core (Figure 5c) working face, respectively.

It is evident that when the excavation face enters the fault core, the contour lines become flatter, with the slope approaching zero, indicating that $p'_x(x_0, y_0) \rightarrow 0$. Simultaneously, as the tunnel is approached ($y \rightarrow 0$), the gradient component $p'_y(x_0, y_0)$ of the contour lines L_i^{DZ}, L_i^{FC} both approaches 0. Therefore, the magnitude of the pore pressure gradient vector at the fault core is smaller than that in the damage zone. This suggests that the variation of pore pressure decreases as the excavation face approaches the fault core.

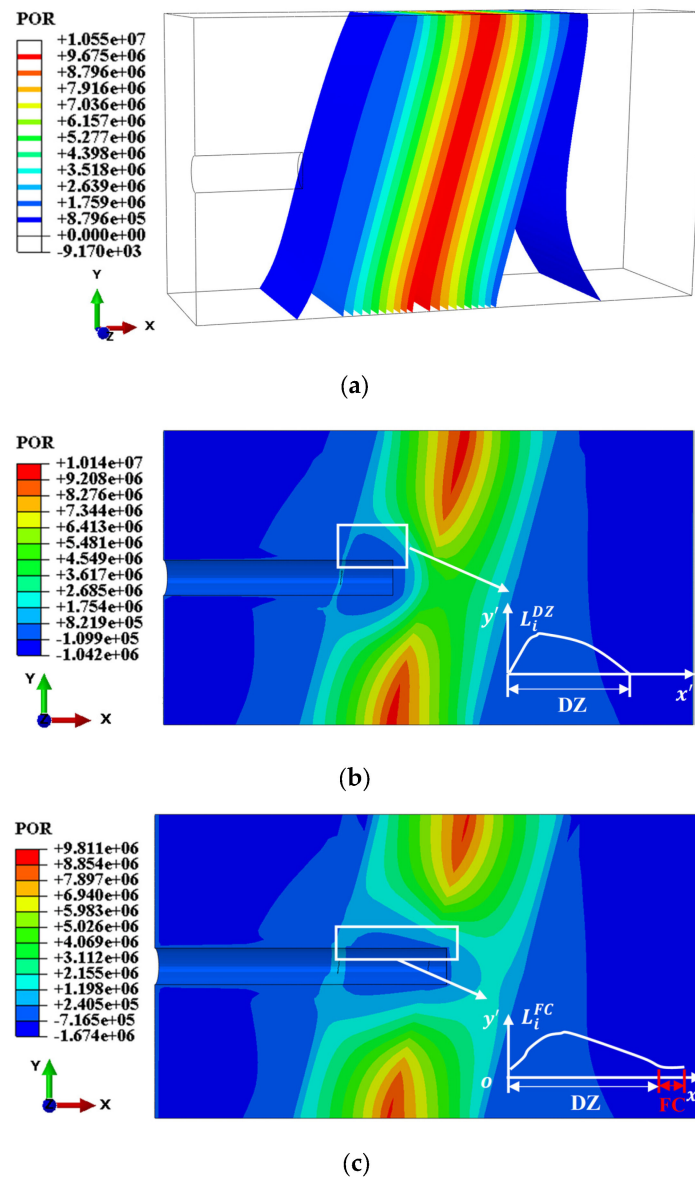


Figure 5. Numerical calculations of the seepage pressure field in the fault zone: (a) contour plot of the seepage pressure distribution within the fault in the undisturbed stage; (b) cloud plot of the seepage pressure distribution and pressure drop equivalent curve L_i^{DZ} when $x = 70$ m; (c) cloud plot of the seepage pressure distribution and pressure drop equivalent curve L_i^{FC} when $x = 90$ m.

5.2. Evolution Law of Velocity

5.2.1. Maximum Water Velocity Change Rule with Advance Length

Transient seepage calculations were conducted in ABAQUS to analyze the temporal variation of water inrush velocity. The calculations were carried out for a duration of 500,000 s. Figure 6 showcases the cloud maps of water inrush velocity at selected characteristic sections, specifically at $x = 70$ m, $x = 80$ m, $x = 85$ m, and $x = 90$ m, at different characteristic time points ($T = 100$ s, $T = 100,000$ s, $T = 500,000$ s). The lateral changes in Figure 6 reflects the change rule of water inrush velocity with advance length under the same time step. The maximum water inrush velocity (v_{max}) of the tunnel face can reflect the severity of the water-surge accident. It can be seen from Figure 6 that the maximum value of water inrush velocity appears in the initial moment of calculation. Take $T = 100$ s as an example: when $x = 80$ m, $v_{max} = 2.47$ m/s. Conversely, at $x = 90$ m, where the tunnel face intersects with the fault core, v_{max} drops to 0.51 m/s, marking a decrease of 79.3% from the preceding value.

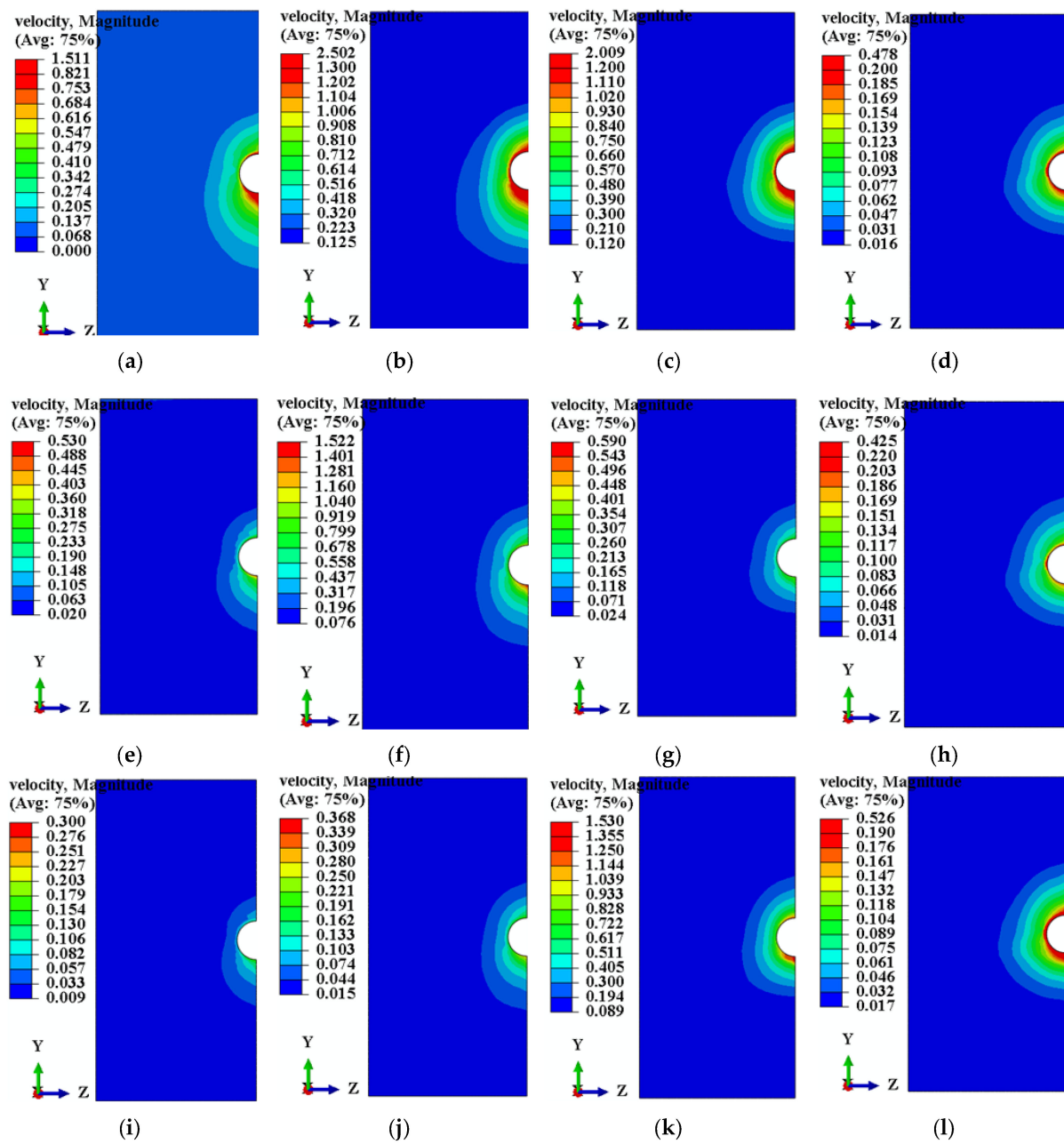


Figure 6. YZ profile cloud diagram of water inrush velocity at tunnel face: (a) $T = 100$ s, $x = 70$ m; (b) $T = 100$ s, $x = 80$ m; (c) $T = 100$ s, $x = 85$ m; (d) $T = 100$ s, $x = 90$ m; (e) $T = 100,000$ s, $x = 70$ m; (f) $T = 100,000$ s, $x = 80$ m; (g) $T = 100,000$ s, $x = 85$ m; (h) $T = 100,000$ s, $x = 90$ m; (i) $T = 500,000$ s, $x = 70$ m; (j) $T = 500,000$ s, $x = 80$ m; (k) $T = 500,000$ s, $x = 85$ m; (l) $T = 500,000$ s, $x = 90$ m.

To visually represent the dynamics of v_{max} , the extremal values from the computational results were extracted, culminating in Figure 7a. This figure illustrates that the maximum water inrush velocity exhibits an initial increase, then decrease, and then increase pattern as the tunnel crosses the heterogeneous fault zone. According to Equation (4), the water inrush velocity is directly proportional to the pore pressure gradient. Insights from Section 5.1 reveal that the pore pressure gradient in the vicinity of the tunnel within the fault core is notably lower compared to that within the damage zone. This discrepancy results in a diminished water inflow rate at the fault core.

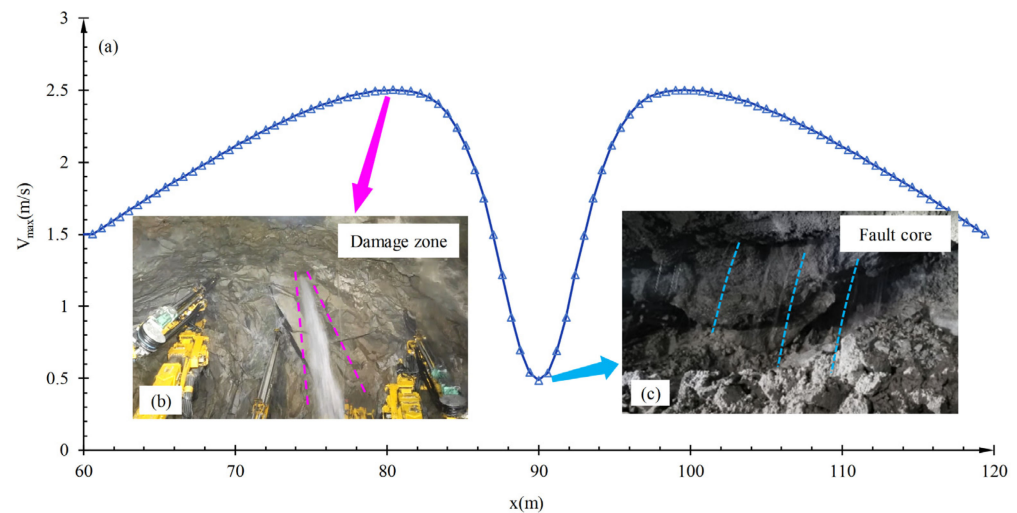


Figure 7. The change of the maximum water inrush velocity v_{max} with the advance length: (a) numerical calculation curve of the v_{max} at the tunnel face as a function of the advance length; (b) on-site real water inrush photos in the damage zone; (c) on-site real water inrush photos in the fault core.

Figure 7b,c showcases photographic evidence of the water inrush event. Figure 7b depicts the damage zone, where several water inrush points can be identified, manifesting as streams and jets with rapid flow rates. By contrast, Figure 7c, captured at the fault core, reveals a higher number of water inrush points, albeit with considerably slower velocities, indicative of a low-speed seepage phenomenon. These visual observations from the field corroborate the numerical simulation outcomes, thereby enhancing the credibility of the research findings.

5.2.2. The Law of Change of Water Inrush Velocity with Time

The longitudinal analysis presented in Figure 6 clearly delineates the temporal variations of water inrush velocity at uniform advance lengths. Meanwhile, Figure 8 reveals how the water inrush velocity evolved over time within the crown across various advance lengths. Notably, in the damage zone, there was a marked reduction in water inrush velocity across different depths as time progressed. For instance, at $x = 70$ m, the velocity decreased from a peak of 1.5 m/s to 0.13 m/s, translating to a reduction rate of 91.3%. In contrast, within the fault core ($x = 90$ m), the water inrush velocity remained remarkably stable, hovering around 0.5 m/s with negligible variation.

Significantly, the distance between the excavation surface and the fault core markedly influences the duration required for the water inflow velocity to stabilize. Specifically, at locations $x = 70$ m, $x = 80$ m, and $x = 85$ m, the time required for the water inrush velocity to decrease from its peak to a steady state is 120,000 s, 250,000 s, and 350,000 s, respectively. This pattern indicates that the nearer the tunnel face is to the fault core, the longer the period for the water inrush velocity to diminish. This analysis can be attributed to the different water storage and supply characteristics between the damage zone and the fault core. The fault core, as the main fracture, provides a water source supply to the damage zone. The closer the excavation face is to the fault core, the stronger the water supply capacity, resulting in a smaller pore pressure gradient and slower velocity reduction.

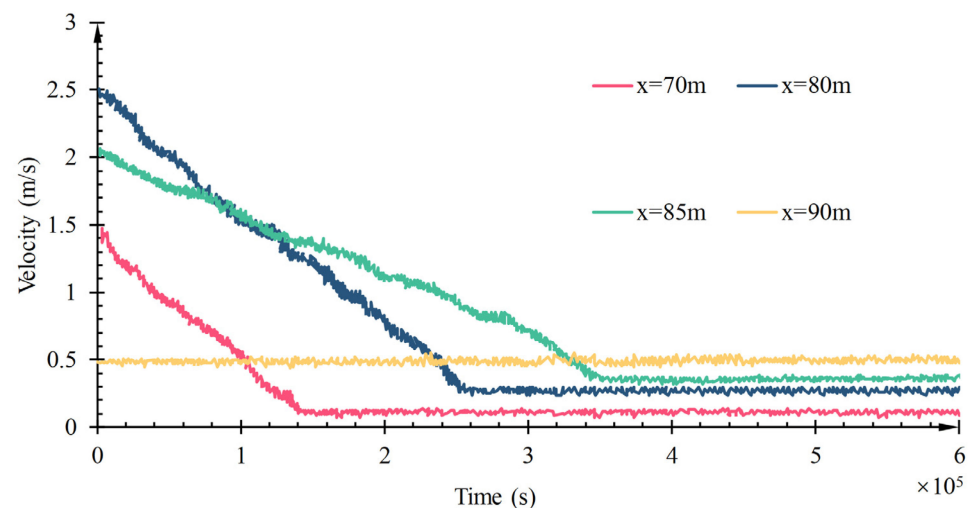


Figure 8. Numerical simulation results of variation of water-surge velocity with time.

5.3. Evolution Law of Water Inflow

5.3.1. Changing Law of Water Influx with Advance Length

In ABAQUS, the Relative Volume Flux (RVF) is utilized to measure the flow velocity at fluid flow boundary nodes, expressed in cubic meters per second (m^3/s). A negative value of RVF signifies outflow from the model. To reflect the variation in water inflow volume with the advance length, the average RVF of the cell grids at each excavation step cross-section is calculated. Figure 9a,b illustrate the variations in water inflow as a function of the advance length at the working face. Specifically, at a depth of $x = 80 \text{ m}$, the water inflow is recorded at $0.79 \text{ m}^3/\text{s}$. However, upon advancing to the fault core at $x = 90 \text{ m}$, the inflow escalates to $1.19 \text{ m}^3/\text{s}$, marking a significant increase of 50.1% from the value at $x = 80 \text{ m}$. As the tunnel face progresses through the fault core, a subsequent decrease in water inflow is observed. This pattern indicates that water inflow typically exhibits a rise followed by a fall, with the peak inflow occurring within the fault core.

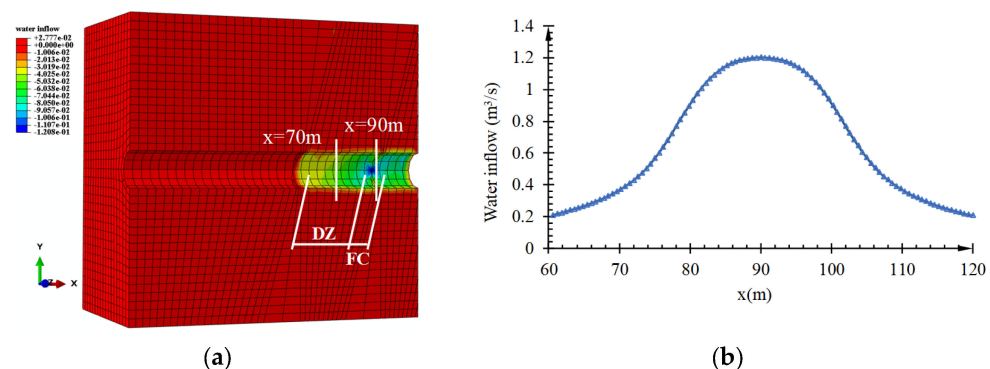


Figure 9. The variation of water inflow with the advance length of the working face: (a) numerical calculation cloud chart of water inflow; (b) curve of water inflow with advance length.

Table 2 lists the on-site water inflow measurements recorded by flow meters connected to the pumping system. To visually depict the trend of water inflow, these data points are represented in the form of Figure 10. Analysis of Figure 10 and Table 2 shows that the pattern of water inflow initially increases and then decreases when crossing a water-rich heterogeneous fault zone. The observed trends are consistent with the results of numerical simulations, thus confirming the accuracy of the numerical model.

Table 2. Daily water inflow field measurement data.

Date	Water Inflow (m ³ /d)									
3–14 March	2982	4616	5127	6139	5319	4047	4714	7918	6172	14,185
15–24 March	9319	6538	9054	13,901	7527	11,910	11,717	11,828	9080	13,146
25 March–3 April	7685	15,258	9487	17,879	14,129	10,374	9580	15,126	15,925	15,944
4–13 April	17,465	8007	17,872	19,258	15,952	14,941	9429	15,038	16,000	13,758
14–23 April	14,547	13,946	16,666	14,516	19,267	22,196	18,952	17,769	20,489	21,787
24 April–3 May	18,594	18,978	20,050	17,009	17,817	18,897	24,132	17,218	18,985	17,706
4–13 May	17,017	19,254	17,180	18,755	18,297	16,654	17,843	19,418	19,267	22,196
14–23 May	13,952	17,769	20,489	21,787	18,594	18,978	20,050	15,009	15,817	16,897
24 May–2 June	24,132	17,218	16,254	17,180	18,755	18,297	16,654	14,843	14,418	19,267
3–12 June	22,196	13,952	17,769	20,489	21,787	11,042	12,231	8807	8273	3248
13–22 June	16,344	8907	10,697	10,001	11,342	9665	14,762	10,880	10,032	8600
23 June–2 July	7915	9258	9774	10,765	10,156	9305	8564	9247	7635	8502
3–12 July	11,829	7865	8807	9354	7384	7504	17,232	15,456	12,437	13,338
13–22 July	11,637	10,539	9148	9765	8582	7541	7856	6519	9459	8258
23 July–1 August	7136	9236	6325	6880	9958	8058	8086	7057	5963	6250
2–11 August	6994	9313	10,576	8192	10,038	8505	9513	7796	7604	10,238
12–21 August	9294	9204	8657	9914	9283	9984	8605	7171	9511	8909
22–31 August	8959	9369	8771	9006	8013	10,730	8257	8256	7064	7407
1–10 September	4685	6802	6690	5720	7347	8623	7770	8510	8158	8465

The green shading data represents the daily water inflow at the tunnel face in the fault core.

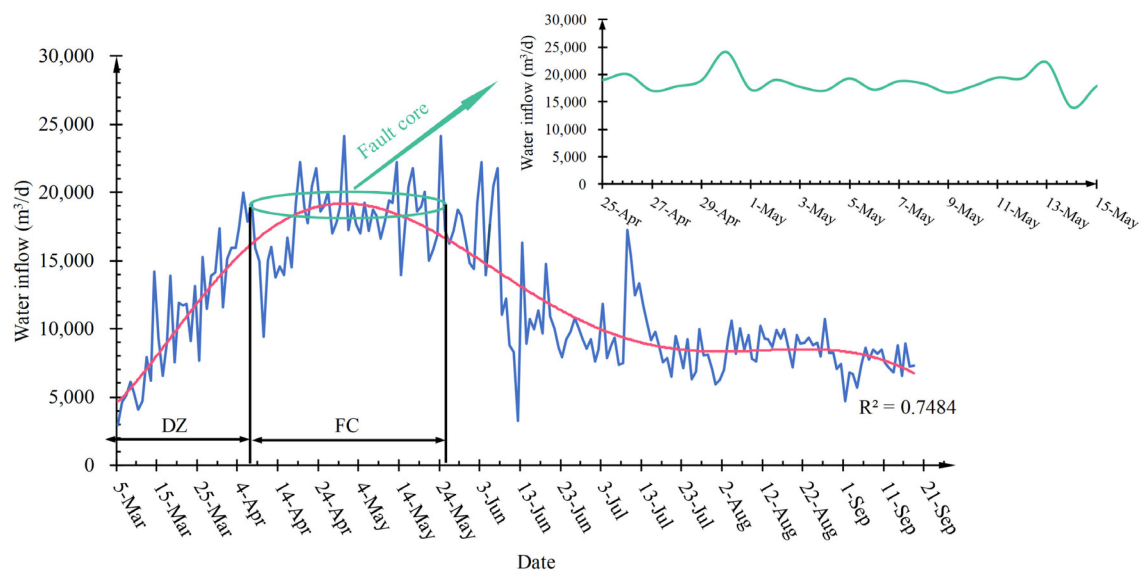


Figure 10. On-site water inflow measurements recorded by flow meters connected to the pumping system between May and September.

5.3.2. The Law of Change of Gushing Water with Time

Figure 11 illustrates the temporal variation in water inflow over a transient analysis period set to 200,000 s, with focus on characteristic cross-sections located at $x = 80$ m within the damage zone and $x = 90$ m inside the fault core. In the damage zone, the water inflow experiences a decline from $0.79 \text{ m}^3/\text{s}$ to $0.23 \text{ m}^3/\text{s}$ as the calculation time extends from 0 to 200,000 s, reflecting a significant reduction of 70.9%. Conversely, within the fault core, the water inflow remains relatively stable throughout the simulation, with minor fluctuations around $1.21 \text{ m}^3/\text{s}$.

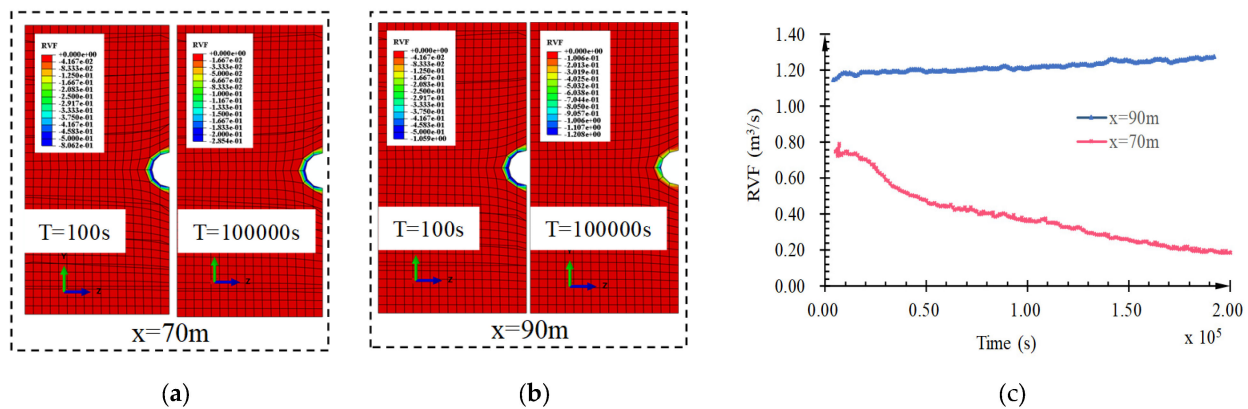


Figure 11. Numerical simulation results of RVF over time: (a) RVF cloud diagram of characteristic time points $T = 100\text{ s}$ and $T = 100,000\text{ s}$ when $x = 70\text{ m}$; (b) RVF cloud diagram of characteristic time points $T = 100\text{ s}$ and $T = 100,000\text{ s}$ when $x = 90\text{ m}$; (c) the change curve of RVF with time when the characteristic advance length is $x = 70\text{ m}$ and $x = 90\text{ m}$.

Figure 10 also displays the daily water inflow values recorded by the flow meter of the on-site drainage pump within the fault core. The daily water inflow data collected from the flow meter connected to the water pump are summarized in the Table 2. An analysis of both Table 2 and Figure 10 reveals that from early March to mid-April, as the tunnel face traversed the damage zone, there was significant short-term fluctuation in daily water inflow. Specifically, on 26 March, the inflow surged to approximately $15,000\text{ m}^3/\text{d}$, then decreased to around $7000\text{ m}^3/\text{d}$ by 27 March. Conversely, from mid-April to early June, once the tunnel reached the fault core, the water inflow remained consistently high, averaging around $20,000\text{ m}^3/\text{d}$. This persistent high inflow necessitated a pause in tunnel construction for about 50 days. The daily water inflow pattern observed when the tunnel crossed the fault fracture zone was consistent with the pattern calculated by numerical simulation, which confirmed the applicability of the model to a certain extent.

6. Discussion

The study reveals two distinct water inrush patterns that occur when crossing water-rich faults in igneous tunnels. The first pattern is characterized by a rapid decrease in water inflow and a short duration when the supply is less than the tunnel inrush flow. This inrush pattern occurs within the fault damage zone, manifesting as a high-speed water inrush. The second pattern occurs when there is a continuous external supply, resulting in a steady inflow and a longer duration. This inrush pattern is found within the fault core, manifesting as a low-speed water inflow. These findings align with the results obtained from tuff injection experiments conducted in hard rock tunnels in Sichuan, China by Ling S., et al. [48]. The results of this study have important implications for the management and mitigation of sudden water hazards in igneous faults.

It is important to highlight that the law derived in this study is applicable specifically to highly heterogeneous faults with a stable external recharge. It should be noted that these types of faults pose significant challenges during construction. Furthermore, this paper primarily focuses on the concept of constructing a non-homogeneous model based on the internal structural properties of the fault. Different engineering situations require specific analysis.

6.1. Water Inrush Mode and Treatment Measures in Damage Zone

The damage zone in the water-rich fault presents a significant hazard in the form of sudden and high water velocities. These high-pressure water jets can extend up to a distance of 5–8 m, posing extreme dangers to personnel and equipment at the construction site (Figure 7b). However, it is important to note that the sudden water velocity decays relatively quickly due to the recharge from the fault core. This decay pattern can be leveraged

by engineers to implement effective measures for managing water inrush. Therefore, we suggest that measures such as adding drainage pumps can be taken to deal with damage zones where a high rate of sudden water is observed. In addition, local grouting can be performed at the outlet once a significant decrease in the rate of water ingress is observed. These measures can maximize the efficiency of the project while ensuring construction safety.

6.2. Water Inrush Mode and Treatment Measures in Fault Core

The main hazard at the nucleus of the fault is the inrush of water that does not decrease over time. Moreover, the long-term water leakage in the fault core can lead to the depletion of fill material within the rock fractures of the tunnel, which can have adverse effects on the mountain ecological environment. To mitigate this, the study suggests the use of the whole-section curtain grouting reinforcement method directly through the fault core. This approach aims to prevent further water leakage and maintain the stability of the tunnel.

The purpose of this paper is to qualitatively analyze the evolution of water inrush in a water-rich fault zone of a rock tunnel and improve the convergence of coupling calculations. To this end, this study has explored some assumptions and simplifications. Specifically, the initial permeability of all parts of the damage zone is assumed to be the same, which simplifies the water inrush process of Darcy flow. However, we must admit that the structural and mechanical behavior of engineering sites is often very complex [23]. Therefore, regarding the water inrush model set up in this paper, although the macroscopic simulation of the water inrush law has been realized, there is still a certain gap between it and the actual situation. Therefore, in future studies, we need to further consider the nonlinear flow variation of faults and the heterogeneity of materials within faults to more accurately reflect the entire water inrush process.

7. Conclusions

A generalized dual porosity fluid-solid coupling model was developed based on the internal tectonic characteristics and hydrodynamic properties of a fault zone. Combining numerical simulations and field data analysis, the following main conclusions were drawn:

- (1) Different evolutionary patterns were observed between the damage zone and the fault nucleation water in the tunnel. In the damage zone, water inrushes were generated quickly and relatively small, decreasing with time. In contrast, fault core water inrush exhibited relatively large and stable outbursts that did not change over time.
- (2) Based on the evolutionary behavior of the igneous faults, targeted preventive and control measures were implemented for other faults in the tunnel. Specifically, local grouting was carried out in the damage zone, while water plugging was carried out using full-section curtain grouting near the fault core.

Author Contributions: Methodology, G.X. and B.W.; Software, G.X.; Investigation, G.X. and H.Z.; Resources, B.W.; Data curation, H.Z. and L.Z.; Writing—original draft, G.X.; Writing—review & editing, X.Y.; Visualization, X.Y.; Supervision, B.W.; Funding acquisition, B.W. All authors have read and agreed to the published version of the manuscript.

Funding: This paper was supported by the National Natural Science Foundation of China (No. 42174165) and Natural Science Foundation of Jiangsu Province (No. BK20230197).

Institutional Review Board Statement: Not applicable.

Informed Consent Statement: Not applicable.

Data Availability Statement: The original contributions presented in the study are included in the article, further inquiries can be directed to the corresponding author.

Acknowledgments: The authors appreciate the reviewers and editors for their time on this paper.

Conflicts of Interest: Author Xinxin Yang was employed by the company Beijing Urban Construction Design & Development Group Co., Limited. The remaining authors declare that the research was

conducted in the absence of any commercial or financial relationships that could be construed as a potential conflict of interest.

References

- Chen, Z.; He, C.; Yang, W.; Guo, W.; Li, Z.; Xu, G. Impacts of geological conditions on instability causes and mechanical behavior of large-scale tunnels: A case study from the Sichuan–Tibet highway, China. *Bull. Eng. Geol. Environ.* **2020**, *79*, 3667–3688. [\[CrossRef\]](#)
- Meng, L.; Li, T.; Jiang, Y.; Wang, R.; Li, Y. Characteristics and mechanisms of large deformation in the Zhegu mountain tunnel on the Sichuan–Tibet highway. *Tunn. Undergr. Space Technol.* **2013**, *37*, 157–164. [\[CrossRef\]](#)
- Xia, L.; Li, M.; Chen, Y.; Zheng, Y.; Yu, Q. Blockiness level of rock mass around underground powerhouse of Three Gorges Project. *Tunn. Undergr. Space Technol.* **2015**, *48*, 67–76. [\[CrossRef\]](#)
- Zhao, K.; Janutolo, M.; Barla, G.; Chen, G. 3D simulation of TBM excavation in brittle rock associated with fault zones: The Brenner Exploratory Tunnel case. *Eng. Geol.* **2014**, *181*, 93–111. [\[CrossRef\]](#)
- Scibek, J.; Gleeson, T.; McKenzie, J.M. The biases and trends in fault zone hydrogeology conceptual models: Global compilation and categorical data analysis. *Geofluids* **2016**, *16*, 782–798. [\[CrossRef\]](#)
- Scibek, J. Multidisciplinary database of permeability of fault zones and surrounding protolith rocks at world-wide sites. *Sci. Data* **2020**, *7*, 95. [\[CrossRef\]](#) [\[PubMed\]](#)
- Crider, J.G. The initiation of brittle faults in crystalline rock. *J. Struct. Geol.* **2015**, *77*, 159–174. [\[CrossRef\]](#)
- Lan, H.; Peng, J.; Zhu, Y.; Li, L.; Pan, B.; Huang, Q.; Li, J.; Zhang, Q. Research on geological and surfacial processes and major disaster effects in the Yellow River Basin. *Sci. China Earth Sci.* **2022**, *65*, 234–256. [\[CrossRef\]](#)
- Masset, O.; Loew, S. Hydraulic conductivity distribution in crystalline rocks, derived from inflows to tunnels and galleries in the Central Alps, Switzerland. *Hydrogeol. J.* **2010**, *18*, 863–891. [\[CrossRef\]](#)
- KC, D.; Gautam, K.; Dangi, H.; Kadel, S.; Hu, L. Challenges in Tunneling in the Himalayas: A Survey of Several Prominent Excavation Projects in the Himalayan Mountain Range of South Asia. *Geotechnics* **2022**, *2*, 802–824. [\[CrossRef\]](#)
- Nilsen, B. Characteristics of Water Ingress in Norwegian Subsea Tunnels. *Rock Mech. Rock Eng.* **2014**, *47*, 933–945. [\[CrossRef\]](#)
- Holmøy, K.H.; Nilsen, B. Significance of Geological Parameters for Predicting Water Inflow in Hard Rock Tunnels. *Rock Mech. Rock Eng.* **2014**, *47*, 853–868. [\[CrossRef\]](#)
- Dahlø, T.S.; Nilsen, B. Stability and rock cover of hard rock subsea tunnels. *Tunn. Undergr. Space Technol.* **1994**, *9*, 151–158. [\[CrossRef\]](#)
- Xu, X.; Jing, H.; Zhao, Z.; Yin, Q.; Li, J.; Li, H. Physical model experiment research on evolution process of water inrush hazard in a deep-buried tunnel containing the filling fault. *Environ. Earth Sci.* **2022**, *81*, 488. [\[CrossRef\]](#)
- Zhang, Q.; Jiang, Q.; Zhang, X.; Wang, D. Model test on development characteristics and displacement variation of water and mud inrush on tunnel in fault fracture zone. *Nat. Hazards* **2019**, *99*, 467–492. [\[CrossRef\]](#)
- Huang, Z.; Zeng, W.; Wu, Y.; Li, S.; Zhao, K. Experimental investigation of fracture propagation and inrush characteristics in tunnel construction. *Nat. Hazards* **2019**, *97*, 193–210. [\[CrossRef\]](#)
- Kong, D.; Gao, Y.; Sarma, H.; Li, Y.; Guo, H.; Zhu, W. Experimental investigation of immiscible water-alternating-gas injection in ultra-high water-cut stage reservoir. *Adv. Geo-Energy Res.* **2021**, *5*, 139–152. [\[CrossRef\]](#)
- Shao, J.; Zhang, W.; Wu, X.; Lei, Y.; Wu, X. Rock Damage Model Coupled Stress-Seepage and Its Application in Water Inrush from Faults in Coal Mines. *ACS Omega* **2022**, *7*, 13604–13614. [\[CrossRef\]](#)
- Wang, J.A.; Park, H.D. Coal mining above a confined aquifer. *Int. J. Rock Mech. Min. Sci.* **2003**, *40*, 537–551. [\[CrossRef\]](#)
- Yang, T.H.; Liu, J.; Zhu, W.C.; Elsworth, D.; Tham, L.G.; Tang, C.A. A coupled flow-stress-damage model for groundwater outbursts from an underlying aquifer into mining excavations. *Int. J. Rock Mech. Min. Sci.* **2007**, *44*, 87–97. [\[CrossRef\]](#)
- Yang, W.M.; Fang, Z.D.; Wang, H.; Li, L.P.; Shi, S.S.; Ding, R.S.; Bu, L.; Wang, M.X. Analysis on Water Inrush Process of Tunnel with Large Buried Depth and High Water Pressure. *Processes* **2019**, *7*, 134. [\[CrossRef\]](#)
- Zhang, J.; Li, S.; Zhang, Q.; Zhang, X.; Li, P.; Wang, D.; Weng, X. Mud inrush flow mechanisms: A case study in a water-rich fault tunnel. *Bull. Eng. Geol. Environ.* **2019**, *78*, 6267–6283. [\[CrossRef\]](#)
- Xie, Q.; Cao, Z.L.; Sun, W.C.; Fumagalli, A.; Fu, X.; Wu, Z.H.; Wu, K. Numerical simulation of the fluid-solid coupling mechanism of water and mud inrush in a water-rich fault tunnel. *Tunn. Undergr. Space Technol.* **2023**, *131*, 104796. [\[CrossRef\]](#)
- Wu, J.; Li, S.C.; Xu, Z.H. Numerical analysis of gas-liquid two-phase flow after water inrush from the working face during tunnel excavation in a karst region. *Bull. Eng. Geol. Environ.* **2019**, *78*, 2973–3010. [\[CrossRef\]](#)
- Hongyun, F.; Liping, L.; Guangqi, C.; Hongliang, L.; Jingyao, G.; Changze, L.; Xinyan, P.; Shen, Z. Analysis method of the water inrush and collapse in jointed rock mass tunnels: A case study. *Eng. Anal. Bound. Elem.* **2023**, *146*, 838–850. [\[CrossRef\]](#)
- Faulkner, D.R.; Jackson, C.A.L.; Lunn, R.J.; Schlische, R.W.; Shipton, Z.K.; Wibberley, C.A.J.; Withjack, M.O. A review of recent developments concerning the structure, mechanics and fluid flow properties of fault zones. *J. Struct. Geol.* **2010**, *32*, 1557–1575. [\[CrossRef\]](#)
- Rawling, G.C.; Goodwin, L.B.; Wilson, J.L. Internal architecture, permeability structure, and hydrologic significance of contrasting fault-zone types. *Geology* **2001**, *29*, 43–46. [\[CrossRef\]](#)
- Shipton, Z.K.; Cowie, P.A. Damage zone and slip-surface evolution over μm to km scales in high-porosity Navajo sandstone, Utah. *J. Struct. Geol.* **2001**, *23*, 1825–1844. [\[CrossRef\]](#)

29. Chester, F.M.; Logan, J.M. Implications for mechanical properties of brittle faults from observations of the Punchbowl fault zone, California. *Pure Appl. Geophys. Pageoph* **1986**, *124*, 79–106. [\[CrossRef\]](#)
30. Caine, J.S.; Evans, J.P.; Forster, C.B. Fault zone architecture and permeability structure. *Geology* **1996**, *24*, 1025–1028. [\[CrossRef\]](#)
31. Balsamo, F.; Storti, F.; Salvini, F.; Silva, A.T.; Lima, C.C. Structural and petrophysical evolution of extensional fault zones in low-porosity, poorly lithified sandstones of the Barreiras Formation, NE Brazil. *J. Struct. Geol.* **2010**, *32*, 1806–1826. [\[CrossRef\]](#)
32. Shipton, Z.K.; Evans, J.P.; Robeson, K.R.; Forster, C.B.; Snelgrove, S. Structural heterogeneity and permeability in faulted eolian sandstone: Implications for subsurface modeling of faults. *AAPG Bull.* **2002**, *86*, 863–883.
33. Perello, P.; Baietto, A.; Burger, U.; Skuk, S. Excavation of the Aica-Mules pilot tunnel for the Brenner base tunnel: Information gained on water inflows in tunnels in granitic massifs. *Rock Mech. Rock Eng.* **2014**, *47*, 1049–1071. [\[CrossRef\]](#)
34. Liu, J.-Q.; Sun, Y.-K.; Li, C.-j.; Yuan, H.-l.; Chen, W.-Z.; Liu, X.-Y.; Zhou, X.-S. Field monitoring and numerical analysis of tunnel water inrush and the environmental changes. *Tunn. Undergr. Space Technol.* **2022**, *122*, 104360. [\[CrossRef\]](#)
35. Wu, J.; Wang, X.; Wu, L.; Lu, Y.-N.; Han, Y.-H. Numerical simulation of water inrush in a tunnel crossing faults: Impacts of fault width, damage zone width, and fault permeability. *Arab. J. Geosci.* **2022**, *15*, 540. [\[CrossRef\]](#)
36. Cheng, L.S. *Advanced Seepage Mechanics*; Petroleum Industry Press: Beijing, China, 2011.
37. Louis, C. *Rock Hydraulics in Rock Mechanics*; Springer: New York, NY, USA, 1974.
38. Choi, J.-H.; Edwards, P.; Ko, K.; Kim, Y.-S. Definition and classification of fault damage zones: A review and a new methodological approach. *Earth-Sci. Rev.* **2016**, *152*, 70–87. [\[CrossRef\]](#)
39. Kim, Y.-S.; Peacock, D.C.P.; Sanderson, D.J. Fault damage zones. *J. Struct. Geol.* **2004**, *26*, 503–517. [\[CrossRef\]](#)
40. Dong, S.; Yi, X.; Feng, W. Quantitative Evaluation and Classification Method of the Cataclastic Texture Rock Mass Based on the Structural Plane Network Simulation. *Rock Mech. Rock Eng.* **2019**, *52*, 1767–1780. [\[CrossRef\]](#)
41. Yan, X.; Huang, Z.Q.; Yao, J.; Zhang, Z.; Liu, P.Y.; Li, Y.; Fan, D.Y. Numerical simulation of hydro-mechanical coupling in fractured vuggy porous media using the equivalent continuum model and embedded discrete fracture model. *Adv. Water Resour.* **2019**, *126*, 137–154. [\[CrossRef\]](#)
42. Teutsch, G. An extended double-porosity concept as a practical modeling approach for karstified terranes. In *Hydrogeological Processes in Karst Terranes: Proceedings of the International Symposium and Field Seminar, Antalya, Turkey, 7–17 October 1990*; IAHS Publication: Oxfordshire, UK, 1990; Volume 207.
43. Moonen, P.; Carmeliet, J. 4—Modelling moisture transport in intact and fractured concrete. In *Understanding the Tensile Properties of Concrete*; Weerheijm, J., Ed.; Woodhead Publishing: Cambridge, UK, 2013; pp. 98–122e. [\[CrossRef\]](#)
44. Miao, T.; Yang, S.; Long, Z.; Yu, B. Fractal analysis of permeability of dual-porosity media embedded with random fractures. *Int. J. Heat Mass Transf.* **2015**, *88*, 814–821. [\[CrossRef\]](#)
45. Ofterdinger, U.S.; Balderer, W.; Loew, S.; Renard, P. Environmental isotopes as indicators for ground water recharge to fractured granite. *Ground Water* **2004**, *42*, 868–879. [\[PubMed\]](#)
46. Hoek, E.; Brown, E.T. The Hoek–Brown failure criterion and GSI—2018 edition. *J. Rock Mech. Geotech. Eng.* **2019**, *11*, 445–463. [\[CrossRef\]](#)
47. Romano, V.; Bigi, S.; Carnevale, F.; De'Haven Hyman, J.; Karra, S.; Valocchi, A.J.; Tartarello, M.C.; Battaglia, M. Hydraulic characterization of a fault zone from fracture distribution. *J. Struct. Geol.* **2020**, *135*, 104036. [\[CrossRef\]](#)
48. Ling, S.; Ren, Y.; Wu, X.; Zhao, S.; Qin, L. Study on Reservoir and Water Inrush Characteristic in Nibashan Tunnel, Sichuan Province, China. In *Proceedings of Engineering Geology for Society and Territory, Turin, Italy, 15–19 September 2015*; Springer: Cham, Switzerland, 2015; Volume 6, pp. 577–582.

Disclaimer/Publisher's Note: The statements, opinions and data contained in all publications are solely those of the individual author(s) and contributor(s) and not of MDPI and/or the editor(s). MDPI and/or the editor(s) disclaim responsibility for any injury to people or property resulting from any ideas, methods, instructions or products referred to in the content.